Optimization of Multi-Subband Parallel and Signal Reconstruction for Remote Sensing Satellite Data Transmission

Ze Wang, Fangmin He, Zhong Yang, Yunshuo Zhang, Jin Meng, and Yaxing Li

***Abstract*—The remote sensing satellite is developing toward high resolution, large data capacity, and fast transmission rate. The ground receiver is correspondingly required to have the high parallel to improve real-time reception and processing capabilities. In the frequency domain, the parallel processing of multiple subbands is achieved by dividing broadband into narrow bands. However, narrow-band subbands are reconstructed into broadband signals, which can lead to cross-subband distortion. It will affect the accuracy of high-resolution remote sensing images. In this article, the subband division and reconstruction framework is proposed by combining the analog filter with the digital filter. The phase calibration methods and digital filter optimization are proposed to improve the amplitude and phase consistency of the reconstructed signal. The simulation results show that the proposed amplitude consistency optimization method effectively reduces the reconstruction error within 0.001 dB. The proposed phase calibration method effectively reduces the bit error rate of the reconstructed signal. The maximum deviation is no more than 0.1%. Experiments have shown that the optimization method can reduce the distortion error of high-resolution remote sensing images.**

***Index Terms*—Amplitude and phase consistency optimization, high resolution, multi-subbands parallel processing, remote sensing satellites, signal reconstruction.**

I. Introduction

With the development of high-resolution satellite remote sensing technology, the quality of remote sensing information has been greatly improved, which means that the amount of data processed is also increasing [1], [2]. American advanced remote sensing satellite Keyhole-12 has a ground resolution as high as 0.1 m, and the real-time data transmission reaches the order of Gbps [3]. The remote sensing satellite is developing toward high resolution, large data capacity, and fast transmission rate [4], [5]. Therefore, the ground receiver should also have real-time receiving and processing capabilities.

However, large bandwidth remote sensing satellite data transmission will inevitably lead to the extremely high data sampling rate at the receiver [6], [7]. In this high-speed environment, even a simple filtering operation will lead to the saturation of the hardware processing module, which cannot meet the requirements of real-time demodulation [8], [9]. Therefore, the high parallel of the demodulation module of remote sensing satellite data ground receiver has become an inevitable development trend.

The subband division and reconstruction technology has the capability of multi-subband parallel processing [10], which is widely used in electronic reconnaissance [11], wideband radar reception [12], [13], and communication antijamming [14], [15]. Remote sensing satellite ground receivers use subband division and reconstruction technology to divide the wideband received signal into multiple subbands. Compared with the original received signal, subband processing can effectively reduce the signal processing rate. Each subband signal recovers the full-band signal through reconstruction technology for subsequent data processing.

However, while subband division improves the processing speed of high-resolution remote sensing images, it may lead to distortion for cross-subband reconstructed signal. The analysis and synthesis filter banks are used for subband division and reconstruction of broadband signals, respectively [16]. When the frequency of the satellite downlink signal is in the filter transition band, the inconsistent amplitude and phase can cause the reconstructed signal distortion, reduce demodulation performance, and lead to image distortion.

A dual-channel orthogonal mirror filter bank proposed in [17] can effectively eliminate aliasing and phase distortion between adjacent subbands. However, the orthogonal mirror filter bank still introduces small amplitude distortion for the reconstructed signal. The multiple-channel polyphase filter banks that greatly simplify the filter design have been introduced since dual-channel orthogonal mirror filter banks [18]. In [19], according to the distortion-free reconstruction theory [20], the subband analysis and synthesis filter banks are designed to eliminate the reconstruction error. The nonuniform discrete Fourier transform modulation filter banks are designed in [21] and the reconstruction and frequency characteristics are analyzed. The

Manuscript received 14 September 2023; revised 6 November 2023; accepted 15 November 2023. Date of current version 15 December 2023. This work was supported in part by the National Key Research and Development Program of China under Grant 2021YFF1500100, in part by the National Natural Science Foundation of China under Grant 52177012, in part by National Defense Science and Technology Key Laboratory Fund under Grant 614221722051301, and in part by the China National Funds for Distinguished Young Scientists under Grant 52025072. *(Corresponding author: Yaxing Li.)*

The authors are with the National Key Laboratory of Electromagnetic Energy, Naval University of Engineering, Wuhan 430033, China (e-mail: d22180818@nue.edu.cn; hefangmin82@gmail.com; yangzhong_yz@hotmail.com; gudaowork@163.com; mengjinemc@163.com; whhit173@hotmail.com).

Digital Object Identifier 10.1109/JSTARS.2023.3335301

© 2023 The Authors. This work is licensed under a Creative Commons Attribution-NonCommercial-NoDerivatives 4.0 License. For more information, see https://creativecommons.org/licenses/by-nc-nd/4.0/

filter optimization criteria prioritize ensuring the flatness of the passband and the attenuation of the stopband, with lower weights for the transition band. Patel et al. [22] adopt a subband parallel and reconstruction method based on weighted overlapping additive structure filter banks. When designing the prototype filter, the power complementarity characteristic was not included as a strong constraint in the mathematical optimization formula, which can result in significant transition band reconstruction errors.

Two typical modulation filter banks, i.e., cosine modulation and complex exponential modulation have been studied in [23], [24], [25], and [26]. By analyzing the distortion-free reconstruction conditions, the design of filter banks design is transformed into the prototype filter. In [27], [28], [29], and [30], the optimization and window function methods that can reduce inter-subband reconstruction errors further are utilized to optimize the design of prototype filters.

The main contributions of this article are given as follows.

1) The multi-subband parallel processing framework for the remote sensing satellite receiver is introduced in this article. To improve the real-time processing speed, a hybrid two-stage subband division scheme with analog circuits and digital filter processing is proposed to divide the broadband signal into processing subbands with the narrower bandwidth.
2) The broadband signal reconstruction modeling is constructed for the hybrid two-stage subband division scheme with analog circuits and digital filter processing. Meanwhile, the influencing factors of amplitude and phase inconsistency in cross-subband signal reconstruction are analyzed in the frequency domain.
3) The phase calibration methods and digital filter design are proposed to improve the amplitude and phase consistency of the reconstructed signal across subbands. The optimization can reduce the error rate of remote sensing satellite data transmission and improve the accuracy of high-resolution remote sensing images.

The rest of this article is organized as follows. Section II introduces the multi-subband parallel processing and reconstruction framework. Section III obtains the influencing factors of signal reconstruction through time-domain modeling and frequency-domain amplitude and phase characteristics analysis. Section IV proposes the filter amplitude–frequency optimization and the phase calibration method, which solves the amplitude and phase distortion from amplitude and phase, respectively. The numerical simulation in Section V verifies that the inconsistency between amplitude and phase leads to the distortion of the reconstructed signal. The method proposed can effectively reduce the reconstruction error. Section VI uses the measured signal spectrum and remote sensing data to verify that the method proposed can reduce the distortion of remote sensing images caused by cross-subband reconstruction. Section VII is the discussion, which elaborates on the limitations of the study and future exploration areas. Finally, Section VIII concludes this article.

II. Multi-Subband Parallel Processing and Reconstruction Framework

The multi-subband parallel processing and reconstruction framework is shown in Fig. 1, which demonstrates data transmission processes from high-resolution remote sensing satellites to ground receivers. The multi-subband parallel processing and reconstruction include an RF receiving circuit and a digital processing module. In the RF receiving circuit, the preselected analog filters achieve the first-stage subband division of the RF signal, which can effectively reduce the requirements for the A/D sampling rate. In the digital processing module, the digital baseband signal is divided into the second-stage subbands through baseband filtering. It can further improve the speed of subband parallel processing. Finally, the reconstructed signal is transmitted to the demodulation module. Binary encoding is correctly demodulated to obtain remote sensing images. In Fig. 1, A/D represents the analog-to-digital conversion unit, and LNA represents the low-noise amplifier.

To improve the real-time reception and processing speed for high-resolution and high-capacity remote sensing data, the ground receiver uses a hybrid two-stage subband division scheme with analog circuits and digital filter processing to produce subband signals with narrower bandwidth. The subbands need to reconstruct and restore the broadband signal from the divided narrow-band signal and it may lead to distortion across subbands. Thus, the broadband signal reconstruction modeling and amplitude–phase consistency optimization are described in the following sections.

III. Multi-Subbands Parallel and Signal Reconstruction Modeling

The RF receiving circuit and digital processing module are mainly implemented for subband division and signal reconstruction. The amplitude and phase characteristics of the overlapping regions between subbands depend on the link, which is presented in Fig. 2. This article mainly analyzes the impact of subband division and reconstruction on useful signals across subbands.

A. Time-Domain Modeling of Signal Reconstruction

Fig. 2 presents the process of subband division and signal reconstruction. The RF signal $x(t)$ is divided into K channels, and the first subband division is achieved after passing through a preselected filter bank $[\ r_1(t)\quad r_2(t)\quad \cdots\quad r_K(t)\ ]^T$. Each analog subband signal is $[\ s_1(t)\quad s_2(t)\quad \cdots\quad s_K(t)\ ]^T$. The input–output relationship in the RF analog circuit is derived as follows, where $\otimes$ represents the convolution operation, and the range of i is $1 \sim K$

$$s_i(t) = x(t) \otimes r_i(t). \tag{1}$$

We utilize the analog-to-digital conversion unit with a sampling rate of f_{ad} to directly sample the RF analog signal and obtain the input signal $[\ \hat{s}_1(n)\quad \hat{s}_2(n)\quad \cdots\quad \hat{s}_K(n)\ ]^T$ of the digital processing module. The conversion from the continuous-time signal to the digital discrete signal is accomplished as

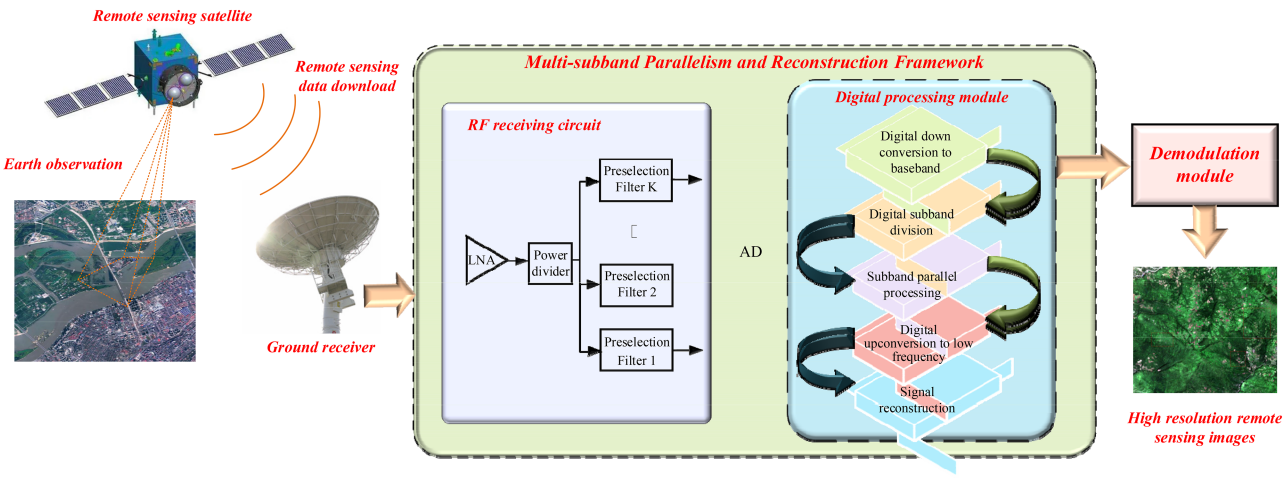

Fig. 1. Multi-subband parallel processing and reconstruction framework.

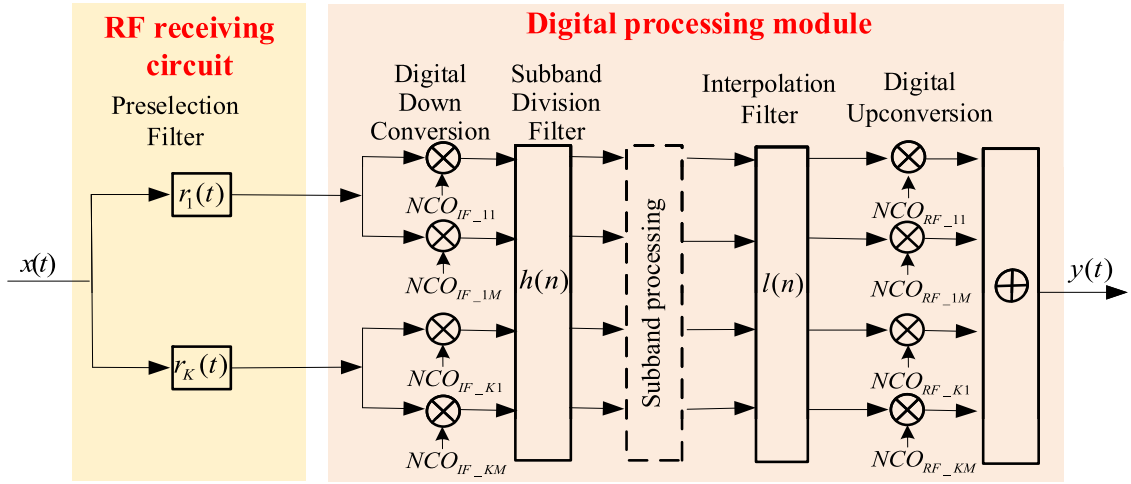

Fig. 2. Mathematical model diagram of multi-subband parallel and signal reconstruction.

follows:

$$\hat{s}_i(n) = s_i(t)|_{t=n/f_{\text{ad}}}. \tag{2}$$

The subband signal $\hat{\boldsymbol{s}}(n)$ of each channel is first divided into M channels, and the baseband signal is obtained through digital downconversion $\boldsymbol{DDC}_{\text{RF}}$. Thereinafter, the subband division filter $h(n)$ performs the second-level subband division of the baseband signal. The high-frequency components caused by interpolation are filtered through an interpolation filter $l(n)$. Afterward, digital upconvert $\boldsymbol{DUC}_{\text{IF}}$ is implemented to obtain a lower carrier frequency. Finally, subbands are synthesize to obtain a reconstructed signal $y(n)$

$$y(n) = [(\hat{\boldsymbol{s}}(n) \times \boldsymbol{DDC}_{\text{RF}}) \otimes h(n) \otimes l(n)] \times \boldsymbol{DUC}_{\text{IF}} \tag{3}$$

where

$$\boldsymbol{DDC}_{\text{RF}} = \begin{bmatrix} \text{DDC}_{\text{RF\_11}} & \cdots & \text{DDC}_{\text{RF\_1}M} \\ \vdots & \ddots & \vdots \\ \text{DDC}_{\text{RF\_}K1} & \cdots & \text{DDC}_{\text{RF\_}KM} \end{bmatrix}_{K\times M} \tag{4}$$

$$\boldsymbol{DUC}_{\text{IF}} = \begin{bmatrix} \text{DUC}_{\text{IF\_11}} & \cdots & \text{DUC}_{\text{IF\_1}M} \\ \vdots & \ddots & \vdots \\ \text{DUC}_{\text{IF\_}K1} & \cdots & \text{DUC}_{\text{IF\_}KM} \end{bmatrix}_{K\times M}. \tag{5}$$

Equations (4) and (5) use digital orthogonal frequency conversion, where the digital downconversion and digital upconversion LO signals for each subband are

$$\text{DDC}_{\text{RF}\_i,j} = e^{j(-2\pi f_{\text{DDC}\_i,j} n + \varphi_{\text{DDC}\_i,j})} \tag{6}$$

$$\text{DUC}_{\text{IF}\_i,j} = e^{j(2\pi f_{\text{DUC}\_i,j} n + \varphi_{\text{DUC}\_i,j})}. \tag{7}$$

In (6) and (7), $j = 1, 2, \ldots, M$. $f_{\text{DDC}\_i,j}$ and $f_{\text{DUC}\_i,j}$ are the local oscillator frequencies of the $K \times M$ subband generated by the connection of digital processing module and the crystal oscillator. $\varphi_{\text{DDC}\_i,j}$ and $\varphi_{\text{DUC}\_i,j}$ are the initial phases of the digital down-converted local oscillator signal and the digital up-converted local oscillator signal, respectively.

B. Analysis of Amplitude and Phase Characteristics in Frequency Domain

In this section, we use the Fourier transform to convert the convolution relationship in the time domain to the product relationship in the frequency domain to intuitively analyze each subbands' amplitude–frequency and phase–frequency characteristics. The frequency-domain expression of (1) is

$$S_i(f) = X(f) \times |R_i(f)| \times e^{j[\varphi_{R\_i}(f)]} \tag{8}$$

where $[\ |R_1(f)|\ \ |R_2(f)|\ \ \cdots\ \ |R_K(f)|\ ]^T$ is the amplitude–frequency response of the preselected filter bank, and $[\ \varphi_{R\_1}(f)\ \ \varphi_{R\_2}(f)\ \ \cdots\ \ \varphi_{R\_K}(f)\ ]^T$ is the phase–frequency response of the preselected filter bank. The design of the filter should satisfy the linear phase condition. Therefore, the relationship between the phase–frequency response and the group delay of the preselected filter is given as follows:

$$\varphi_{R\_i}(f) = 2\pi f \tau_{R\_i} \tag{9}$$

where $[\ \tau_{R\_1}\ \ \tau_{R\_2}\ \ \cdots\ \ \tau_{R\_K}\ ]^T$ is the preselected filter group delay. According to the sampling theorem, the ADC samples the band-limited signal to obtain a digital signal. The frequency-domain expression corresponding to the sampling in (2) is obtained as follows:

$$\hat{S}_i(f) = f_{\text{ad}} \sum_{k=-\infty}^{\infty} S_i(2\pi f - 2k\pi f_{\text{ad}}). \tag{10}$$

After sampling, k means that the original signal spectrum undergoes periodic extension along the frequency axis. In the digital processing module, each subband signal is synthesized into a reconstructed signal. The frequency-domain expression corresponding to (3) can be expanded as follows: where $|H(f)|$ and $\varphi_H(f)$ are the amplitude–frequency response and phase–frequency response of the subband division filter, respectively; $|L(f)|$ and $\varphi_L(f)$ are the amplitude–frequency response and phase–frequency response of the interpolation filter, respectively. N_H and f_H are the order and sampling rate of the subband division filter. N_L and f_L are the order and sampling rate of the interpolation filter. Therefore, the phase–frequency responses of the subband division filter and the interpolation filter are expressed as

$$\varphi_{H}(f) = 2\pi f \frac{N_H}{2f_H} \tag{12}$$

$$\varphi_{L}(f) = 2\pi f \frac{N_L}{2f_L}. \tag{13}$$

The frequency response of the signal reconstruction model is expressed as the sum of the frequency responses of all subbands. The frequency response of each subband consists of amplitude–frequency response $|A_{i,j}(f)|$ and phase–frequency response $\Psi_{i,j}(f)$, which can intuitively evaluate the amplitude–phase characteristics of the reconstructed signal. Therefore, the frequency-domain relationship between the RF input signal and the reconstructed signal is defined as

$$Y(f) = \sum_{i=1}^{K}\sum_{j=1}^{M} |A_{i,j}(f)|\, e^{j\Psi_{i,j}(f)} X(f). \tag{14}$$

The frequency-shifting processes can meet the following relationships:

$$-kf_{\text{ad}} - f_{\text{DDC}\_i,j} + f_{\text{DUC}\_i,j} = \Delta f_c \tag{15}$$

which is the difference between the carrier frequency of the RF input signal and the carrier frequency of the reconstructed signal. Substituting simultaneous (8), (10), (11) shown at the bottom of this page, and (15) into (14)

$$|A_{i,j}(f)| = |R_i(f)| \times |H(f + f_{\text{DUC}\_i,j})| \times |L(f + f_{\text{DUC}\_i,j})| \tag{16}$$

$$\Psi_{i,j}(f) = \varphi_{R\_i}(f) + \varphi_{H}(f + f_{\text{DUC}\_i,j}) + \varphi_{L}(f + f_{\text{DUC}\_i,j}) + \varphi_{\text{DDC}\_i,j} + \varphi_{\text{DUC}\_i,j}. \tag{17}$$

The inconsistent amplitude and phase of adjacent subband overlapping regions can cause the reconstruction distortion of the composite subband signal. The inconsistent relative amplitude of each frequency component in the overlapping region causes amplitude distortion, and the resulting phase shift is not proportional to frequency, resulting in phase distortion.

Assuming that the receiving bandwidth is f_B, the first subband division of the RF circuit yields K analog subbands, and the second subband division of the digital baseband yields $K \times M$ digital subbands. Therefore, the difference between the center frequencies of each analog subband is

$$\Delta f_{\text{RF}} = \frac{f_B}{K}. \tag{18}$$

The difference between the center frequencies of each digital subband corresponds to the frequency difference of the $K \times M$ channel digital upconversion

$$\Delta f_{\text{DUC}} = f_{\text{DUC}\_i,j+1} - f_{\text{DUC}\_i,j} = \frac{f_B}{K \times M}. \tag{19}$$

The phase difference in the overlapping area of adjacent digital subbands can be expressed as

$$\Psi_{i,j+1}(f) - \Psi_{i,j}(f) = 2\pi\Delta f_{\text{DUC}} \frac{N_H}{2f_H} + 2\pi\Delta f_{\text{DUC}} \frac{N_L}{2f_L} + \varphi_{\text{DDC}\_i,j+1} + \varphi_{\text{DUC}\_i,j+1} - \varphi_{\text{DDC}\_i,j} - \varphi_{\text{DUC}\_i,j}. \tag{20}$$

$$Y(f) = \sum_{i=1}^{K}\sum_{j=1}^{M} \left\{ \begin{array}{l} \hat{S}_i(f - f_{\text{DDC}\_i,j} + f_{\text{DUC}\_i,j}) \\ \times |H(f + f_{\text{DUC}\_i,j})| \\ \times |L(f + f_{\text{DUC}\_i,j})| \\ \times e^{j[\varphi_H(f + f_{\text{DUC}\_i,j}) + \varphi_L(f + f_{\text{DUC}\_i,j}) + \varphi_{\text{DDC}\_i,j} + \varphi_{\text{DUC}\_i,j}]} \end{array} \right\} \tag{11}$$

The phase difference in the overlapping area of adjacent analog subbands can be expressed as follows:

$$\Psi_{i+1,1}(f)-\Psi_{i,M}(f)=2\pi[f(\tau_{R\_i+1}-\tau_{R\_i})+\Delta f_{\text{DUC}}\frac{N_H}{2f_H}+\Delta f_{\text{DUC}}\frac{N_L}{2f_L}]+\varphi_{\text{DDC}\_i+1,1}+\varphi_{\text{DUC}\_i+1,1}-\varphi_{\text{DDC}\_i,M}-\varphi_{\text{DUC}\_i,M}. \tag{21}$$

The phase difference in the overlapping regions of adjacent digital subbands is caused by the following factors:

1) the frequency difference of digital frequency conversion;
2) the order and sampling rate of the subband division filter;
3) the order and sampling rate of the interpolation filter;
4) the initial phase of digital frequency conversion.

It only involves the difference in phase–frequency characteristics caused by various links in the digital processing module.

The phase difference in the overlapping area of adjacent analog subbands also includes the time delay of the preselected filter and various segments in the digital processing module.

IV. Amplitude and Phase Consistency Optimization

The frequency response of a fully reconstructed system satisfies the condition that the linear phase and amplitude–frequency response are constant [31], [32]. According to the principle of complete reconstruction, the optimal design of phase consistency and filter amplitude consistency is proposed.

A. Phase Consistency Optimization Design

By analyzing the phase–frequency characteristics of analog and digital subband overlapping regions, design requirements and optimization methods are proposed for the various influencing factors in RF conditioning circuits and digital processing modules. To ensure phase consistency in the overlapping regions of the subbands, the following factors are required.

1) *Group delay design requirements for preselected filter banks:* Each preselected filter is designed to ensure that the group delay is consistent. The group delay equalization optimization method can meet the requirement of $\tau_{R\_i+1}=\tau_{R\_i}$ [33].
2) *Optimal design of subband partitioning filter and interpolation filter orders:* In the digital processing module, the order of the subband division filter and the interpolation filter is designed to satisfy the following formula, where N is an integer:

$$2\pi\Delta f_{\text{DUC}}\frac{N_H}{2f_H}+2\pi\Delta f_{\text{DUC}}\frac{N_L}{2f_L}=2N\pi. \tag{22}$$

3) *Calibration method of interchannel phase difference between digital local oscillator signal initial phase:* By introducing phase compensation, the initial phase problem of digital local oscillator can be solved. According to the above ideas, the phase calibration method is designed as follows.

Algorithm 1: Phase Calibration Method.

Purpose: Solve the phase compensation amount and balance the phases of adjacent subbands.
Input: calibrating signal
Output: Phase compensation amount
step:
(1) $i=1$;
(2) Generate a single-tone calibration signal:
Frequency: $f_0=(f_i+f_{i+1})/2$;
where f_i and f_{i+1} are the center frequencies of the subbands i and $i+1$, respectively;
(3) Inject the calibration signal into the front end of the RF conditioning circuit and enter the subband division and signal reconstruction link;
(4) Before signal reconstruction, the calibration signal spectrum of subbands i and $i+1$ is obtained through a fast Fourier transform;
(5) Extract the complex component with the frequency f_0 in the spectrum, calculate its phases φ_i and φ_{i+1}, and obtain the phase difference $\Delta\varphi=\varphi_{i+1}-\varphi_i$ of adjacent subbands after subtraction;
(6) Calculate the phase compensation amount $e^{j\Delta\varphi}$ to balance the phase shift of the $i+1$ subband;
(7) $i=i+1$;
(8) Repeat steps (2)–(7), until $i=K\times M-1$, where K is the number of analog subbands and M is the number of digital subbands.

B. Optimal Design of Filter Amplitude–Frequency Response

Based on the undistorted phase, this section uses a method of overlapping the passbands of preselected filters in adjacent analog subbands so that the digital subband overlap region is within the passband of the analog filter. It can simplify the signal reconstruction amplitude–frequency response to the design of a subband division filter. The subband division filter is designed according to the criterion that the transition band has a cosine roll-off characteristic. It satisfies the complementary amplitude–frequency response of two digital subbands in the overlapping region, thereby achieving amplitude distortion free.

The amplitude–frequency response of each subband in (16) is obtained by multiplying the amplitude–frequency response of a preselected filter, a subband division filter, and an interpolation filter. The passband design of the preselected filter bank determines the division method of the first-level analog subband. According to the division method of the analog subband and digital subband in Fig. 3, the passbands of the preselected filter overlap to a certain extent. Therefore, the amplitude–frequency response design of the overlap region can be simplified to the design of a subband division filter. That is, the condition that the amplitude–frequency response of the subband division filter between adjacent subbands is complementary is satisfied as follows:

$$\sum_{i=1}^{K}\sum_{j=1}^{M}|H(f+f_{\text{DUC}\_i,j})|=1. \tag{23}$$

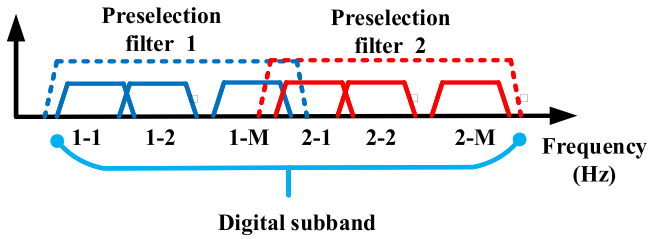

Fig. 3. Schematic diagram of division of analog subband and digital subband.

The subband division filter is a linear phase low-pass filter that can be designed based on an ideal frequency response $H_d(f)$. Its transition band has a square cosine roll-off characteristic

$$H_d(f)=\begin{cases} e^{-j2\pi fN/2} & f\in[0,f_p] \\ \cos^2\left[\frac{\pi}{2\times\Delta f}(f-f_p)\right]\times e^{-j2\pi fN/2} & f\in[f_p,f_s] \\ 0 & f\in[f_s,\pi] \end{cases} \tag{24}$$

where $N/2$ is the filter delay, f_s is the passband cutoff frequency, f_p is the stopband start frequency, and $\Delta f = f_s - f_p$ is the filter bandwidth. Using the idea of optimal approximation to design a subband partition filter $H(f)$, the objective optimization function can be expressed as minimizing the maximum approximation error, i.e., the minimax optimization criterion

$$\text{Minimize} \quad \max(|H(f)-H_d(f)|. \tag{25}$$

Define the basic characteristics of the following three filter designs simultaneously.

1) φ_1 represents stopband attenuation characteristics to prevent aliasing interference between different filters

$$\varphi_1 = \max_{f_s<f<\pi}|H(f)|. \tag{26}$$

2) φ_2 represents the passband flatness characteristic, ensuring the amplitude flatness of the passband

$$\varphi_2 = \max_{0<f<f_p}|H(f)|-1. \tag{27}$$

3) φ_3 represents the amplitude distortion-free characteristic, the filter band between subbands meets the principle of amplitude complementarity

$$\varphi_3 = \max_{f_p<f<f_s}|H(f-f_m)|+|H(f-f_{m+1})|-1. \tag{28}$$

In (28), $m\in[1,K\times M-1]$, f_m is the center frequency of the mth digital subband, and $H(f-f_m)$ represents the filter response of the prototype filter after upconversion. The spectrum is moved to the position where the center frequency is f_{m+1}. Based on the optimization function, the three characteristics of the reconstruction filter are constrained, and combined with engineering indicators, the threshold values δ, ε, and η of the constraint conditions are designed

$$\text{Subject to}\begin{cases}\varphi_1\le\delta \\ \varphi_2\le\varepsilon \\ \varphi_3\le\eta\end{cases} \tag{29}$$

where δ is used to measure the threshold value of the stopband attenuation characteristic, ε indicates that the fluctuation range of the passband amplitude is within this threshold value, and η corresponds to the allowable reconstruction error in engineering practice. Solve the optimization objective function based on three constraints.

The frequency response of the subband division filter can be expressed as follows:

$$H(f)=\sum_{n=0}^{N-1}h(n)\times e^{-jn2\pi f}=h^T\{c(f)-js(f)\} \tag{30}$$

where $h=[h(0),h(1),\ldots,h(N-1)]^T$ is the time-domain coefficient vector of the filter

$$c(f)=[1,\cos(2\pi f),\ldots,\cos(2\pi(N-1)f)]^T \tag{31}$$

$$s(f)=[0,\sin(2\pi f),\ldots,\sin(2\pi(N-1)f)]^T. \tag{32}$$

The real and imaginary parts of $H_d(f)$ are denoted as $H_{d\_R}(f)$ and $H_{d\_I}(f)$.

After discretization, the filter design problem is transformed into a convex optimization problem

$$\min_h T=||Y-AX||_2. \tag{33}$$

In (33), $||\cdot||_2$ represents the two norms

$$Y=[H_{d\_R}(f)\quad H_{d\_I}(f)]^T \tag{34}$$

$$A=[h^T\quad h^T]^T \tag{35}$$

$$X=[c(f)\quad s(f)]^T. \tag{36}$$

In the design process of the subband division filter, the transition bandwidth, passband ripple, stopband attenuation, and filter order need to be considered in compromise. Generally, by optimizing the transition bandwidth and order, the filter satisfies (29), which satisfies the requirement of reconstruction amplitude consistency.

The dichotomy method is used to search for the transition bandwidth and order, and the iteration is stopped until the step $f_{\text{step}}/N_{\text{step}}$ is smaller than the given step threshold $f_{\text{th}}/N_{\text{th}}$. During optimization, the filter temporal coefficients that satisfy (29) and minimize (33) are found. The subband division filter optimization method is given as follows.

V. Simulation

The simulation uses the frequency range of 700–820 MHz and an RF signal sampling rate of 1.8 GHz.

The filter design's impact on the reconstructed signal's amplitude–frequency response is analyzed first. By using optimization methods, a subband division filter is constructed, which satisfies the amplitude complementarity characteristics of the transition bands. The amplitude distortion error of the reconstructed signal caused by the filter design is analyzed.

Second, the impact of phase inconsistency in the subband overlap region on the reconstruction of cross-subband minimum shift keying (MSK) signals is discussed. And phase calibration methods are used to verify the improvement of phase consistency

Algorithm 2: Subband Division Filter Optimization Algorithm.

Purpose: Optimal Filter Design Under the Joint Constraints of Passband, Transition Band, and Stopband Index Parameters.
Input: Calibrating signal
Output: The filter temporal coefficients $h(n)$ that minimize (33).
step:

(1) Set initial order N_0 and transition bandwidth Δf_0
(2) Design index parameters δ, ε, η
(3) Given step thresholds: f_{th}, N_{th}
(4) calculate φ_1, φ_2, φ_3
(5) $i = 0$
(6) **if** {satisfy (29)} **then**
(7) calculate $T(i)$
(8) $f_{\text{step}} = \Delta f_0$
(9) $\mu = 1$
(10) **while** $\{f_{\text{step}} < f_{\text{th}}\}$ **do**
(11) $\Delta f = \Delta f - \mu f_{\text{step}}/2$
(12) i++
(13) calculate φ_1, φ_2, φ_3, $T(i)$
(14) **if** {satisfy (29)} **then**
(15) $\mu = 1$
(16) **else**
(17) $\mu = -1$
(18) **end if**
(19) **end while**
(20) **else**
(21) $N = 2 * N_0$
(22) $N_{\text{step}} = N/2$
(23) **while** $\{N_{\text{step}} < N_{\text{th}}\}$ **do**
(24) $N = N - \mu N_{\text{step}}/2$
(25) i++
(26) calculate φ_1, φ_2, φ_3, $T(i)$
(27) **if** {satisfy (29)} **then**
(28) $\mu = 1$
(29) **else**
(30) $\mu = -1$
(31) **end if**
(32) **end while**
(33) **end if**
(34) Min $\{T(i)\}$ corresponding $h(n)$

of the reconstructed signal spectrum and time-domain waveform.

Finally, the effects of different phase distortions on communication bit error rate (BER) curves are compared.

A. Filter Design

Perform signal-level simulation based on simulation conditions and design three preselected filters with an overlapping passband bandwidth of 4 MHz. The receiving bandwidth of 120 MHz is evenly divided into three analog subbands. The passband range and center frequency of the preselected filter bank are shown in Table I. Then, each analog subband with a 44-MHz passband bandwidth is divided into two digital subbands through the subband division filter. The subband division filter is designed according to the optimization method, and its parameters are shown in Table II. According to the constraints of (23), the interpolation filter order is set to 180.

TABLE I
PRESELECTED FILTER BANK PASSBAND RANGE AND CENTER FREQUENCY (MHZ)

Number of preselected filter banks	Passband starting frequency	Passband cutoff frequency	Passband center frequency
Preselection filter 1	698	742	720
Preselection filter 2	738	782	760
Preselection filter 3	778	822	800

TABLE II
SUBBAND DIVISION FILTER PARAMETERS

parameter	value
Passband cutoff frequency	9 MHz
Stopband starting frequency	11 MHz
Order	512
Stopband attenuation maximum δ	−110 dB
Passband amplitude flatness ε	0.01 dB
Reconstruction error of transition zone η	0.05 dB

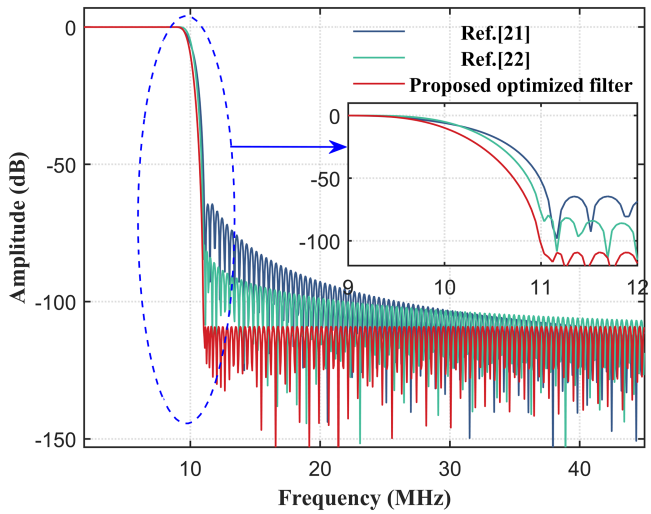

Fig. 4. Normalized power spectrum of the prototype filter.

Fig. 4 shows the comparison of the proposed optimized filter and the prototype filter designed in [21] and [22]. The passband cutoff frequency, stopband start frequency, and order of the three are consistent. The prototype filter optimized and designed in this article meets the constraint conditions. Compared with [21] and [22], it has a greater stopband attenuation and a more pronounced trend of steep descent in the transition zone. It is beneficial for reducing the "bulge" phenomenon in the overlapping zone.

A schematic diagram of three analog subbands divided by three preselected filters and six digital subbands divided by a subband division filter is shown in Fig. 5. The overlapping regions of two analog subbands with 740 and 780 MHz as the

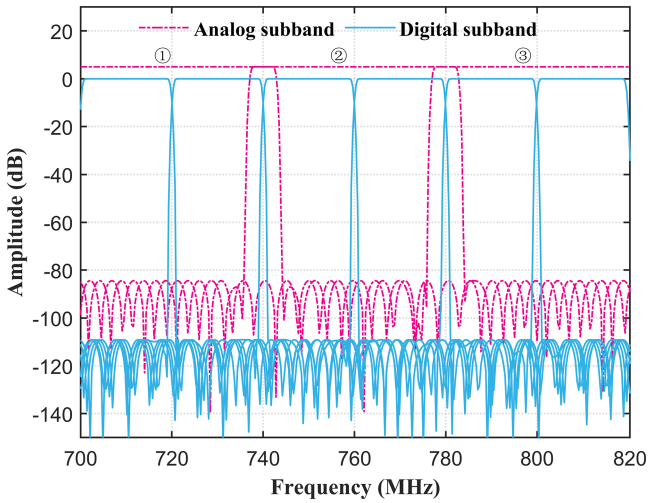

Fig. 5. Analog subband and digital subband division diagram.

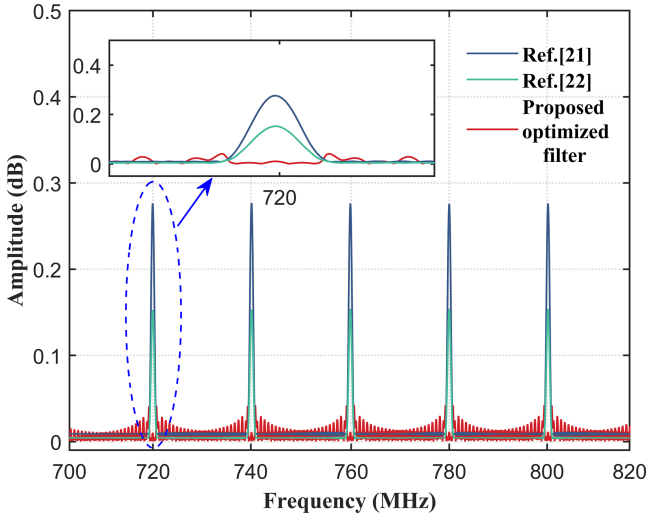

Fig. 6. Filter amplitude–frequency response reconstruction error.

central frequency points are designed to overlap the passbands of adjacent preselected filters. It can ensure that the overlapping regions of the digital subbands are all within the passbands of the analog subbands. Among them, the passband ripple of the digital subband is small enough, mainly considering the impact of the overlapping area of the transition bands of adjacent digital subbands on amplitude consistency.

Fig. 6 shows the amplitude–frequency response reconstruction effect of the entire processing bandwidth. The filter optimized in this article reduces the reconstruction error in the subband overlap area on the premise of losing a certain degree of passband flatness. In combination with the comparison of reconstruction error in Table III, compared with the maximum reconstruction error of 0.28 dB in [21] and 0.17 dB in [22], the filter designed in this article can maintain the full-bandwidth reconstruction mean squared error of 0.0001 dB, with the maximum error not exceeding 0.04 dB. It can achieve high-amplitude consistency across the entire frequency band. It has

TABLE III
COMPARISON OF RECONSTRUCTION ERRORS (FULL BAND 700–820 MHZ)

Prototype Filter	Mean square reconstruction error (dB)	Maximum reconstruction error (dB)
[21]	0.0026	0.28
[22]	0.0015	0.17
Proposed optimized filter	0.0001	0.04

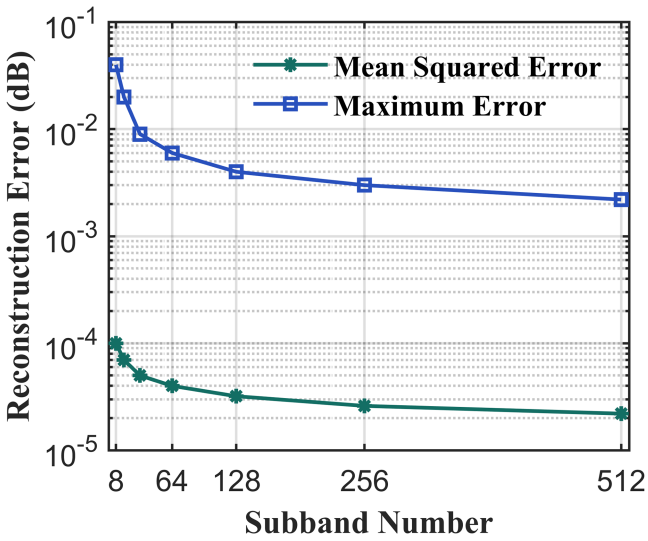

Fig. 7. Relationship between the subband number and reconstruction error.

good stopband attenuation characteristics, flat passband characteristics, and complementary amplitude characteristics between subbands, meeting the requirements of signal reconstruction system amplitude consistency, and can achieve the approximate perfect reconstruction.

The reconstruction performance of filter optimization methods is affected by the number of subbands. Fig. 7 shows the relationship curve between the subband number and reconstruction error. By increasing the subband number, the transition bandwidth will correspondingly decrease. The reconstruction error of the transition band will correspondingly decrease, thus reducing the composite reconstruction error. However, under the same receiving bandwidth, the more subbands there are, the higher the order of the prototype filter. According to filter bank theory, hardware overhead can be measured by the order of the prototype filter. The length of the filter coefficient is directly proportional to the subband number. Therefore, from the perspective of hardware overhead, the subbands number should be minimized as much as possible.

B. Phase Consistency Optimization

Based on the high-amplitude consistency, the reconstruction after the phase consistency optimization is compared through simulation.

The signal reconstruction system is simulated at the signal level using MATLAB. The simulation conditions are set to ensure that the phase of the subband overlap region caused by

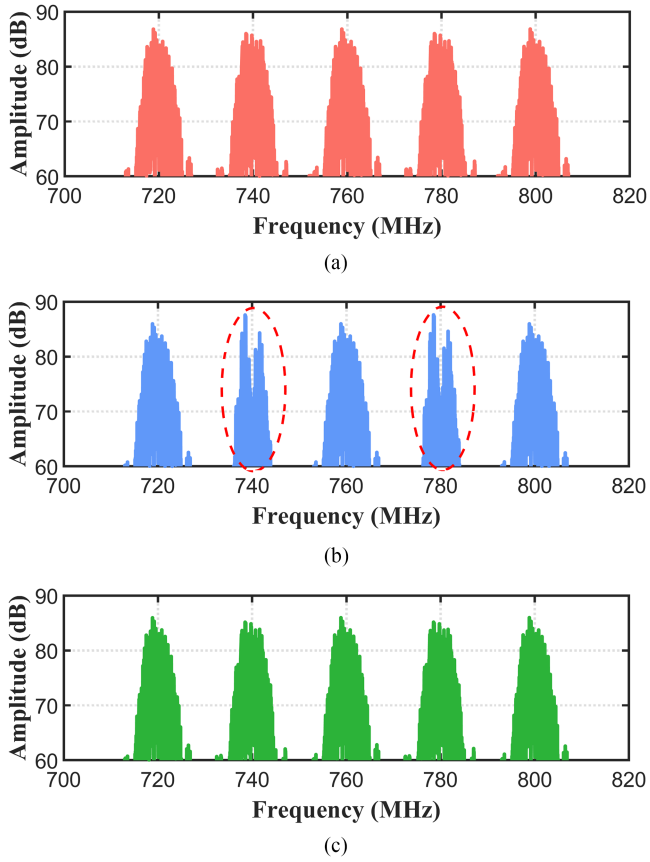

Fig. 8. Spectrum of the reconstructed signal before and after phase consistency optimization. (a) MSK input signal spectrum. (b) Reconstructed signal spectrum with inconsistent phases. (c) Reconstructed signal spectrum after phase consistency optimization.

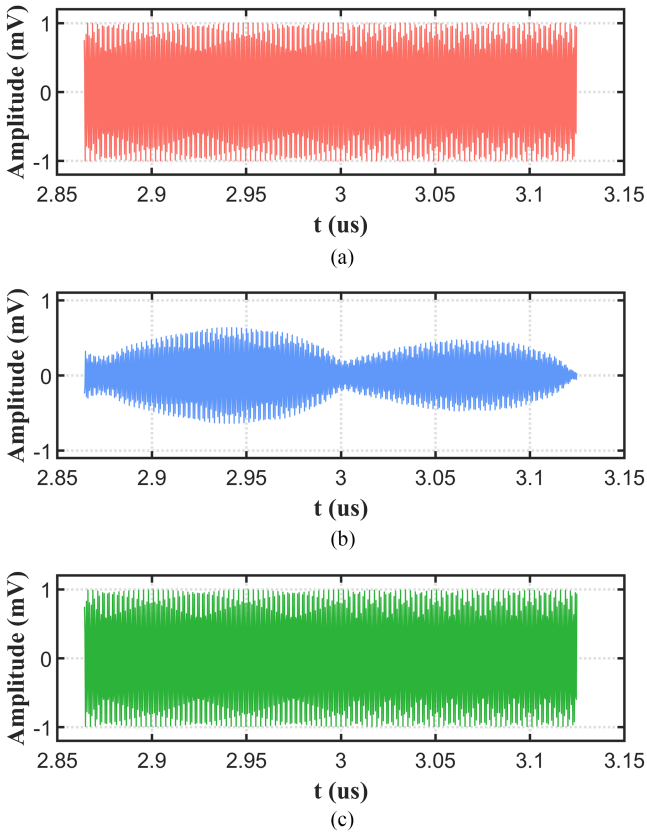

Fig. 9. Time-domain waveform of the reconstructed signal before and after phase consistency optimization. (a) Time-domain waveform of MSK input signal. (b) Time-domain waveform of reconstructed signal with inconsistent phases. (c) Time-domain waveform of the reconstructed signal after phase consistency optimization.

the two variables of preselected filter group delay and digital filter order is consistent. Set the initial phase of the two digital subbands in the analog subband 2 to π, and the initial phase of the digital subbands in the other analog subbands to 0. This setting can result in a phase difference of 180° in the overlapping region of the analog subbands 2 and 1, 3. The input signal uses MSK signals. Its carrier frequencies are 720, 740, 760, 780, and 800 MHz, with a code rate of 8 MHz.

The reconstructed signal spectrum before and after phase consistency optimization is shown in Fig. 8. The original input signal spectrum in Fig. 8(a) comprises five MSK signal spectrums. As shown in Fig. 8(b), the reconstructed signal spectrum at two frequency points, 740 MHz and 780 MHz, is located in the overlapping region of analog subbands. During signal synthesis, phase inversion and amplitude cancellation lead to spectrum distortion, resulting in a "pit" phenomenon. In Fig. 8(c), phase undistorted reconstruction is achieved through the phase calibration method. The reconstructed signal spectrum is almost restored to the original input signal spectrum. It verifies that the phase calibration method can achieve phase balancing of adjacent analog subbands in the overlapping region.

Time-domain waveform of the reconstructed signal before and after phase consistency optimization is shown in Fig. 9. The time-domain waveform of the MSK signal with a carrier frequency of 740 MHz, with a constant envelope characteristic, is shown in Fig. 9(a). The reconstructed signal time-domain waveform with a 180° phase difference between simulated subbands is shown in Fig. 9(b). The time-domain waveform undergoes distortion, which results in the loss of the constant envelope characteristics of the MSK signal. The distortion of the waveform may result in the loss of useful information for transmission. The reconstructed signal time-domain waveform after phase calibration is shown in Fig. 9(c). It restores the signal across the analog subband to the time-domain waveform of the original input MSK signal without phase distortion using a phase calibration method.

C. *Influence of Different Degrees of Phase Distortion on Demodulation Performance*

Optimizing the amplitude and phase consistency of the overlapping subbands minimizes the distortion of the reconstructed signal across subbands. The optimization method can avoid damage to the communication signal and ensure the stability of communication efficiency. Therefore, the impact of different phase distortions is analyzed using the BER curves under different signal-to-noise ratios to measure demodulation performance. Demodulation performance can characterize the accuracy of

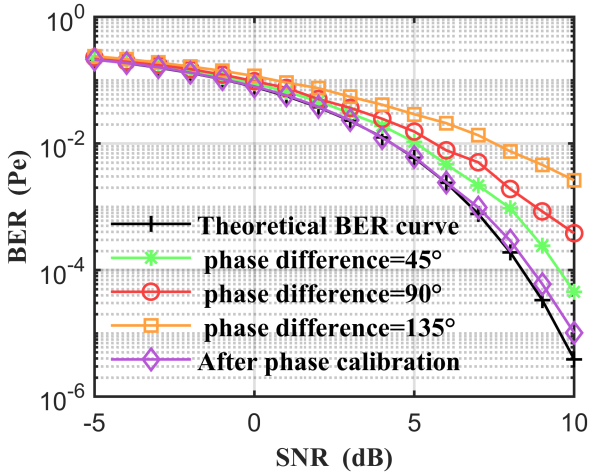

Fig. 10. BER curve of MSK reconstructed signal under different phase distortions.

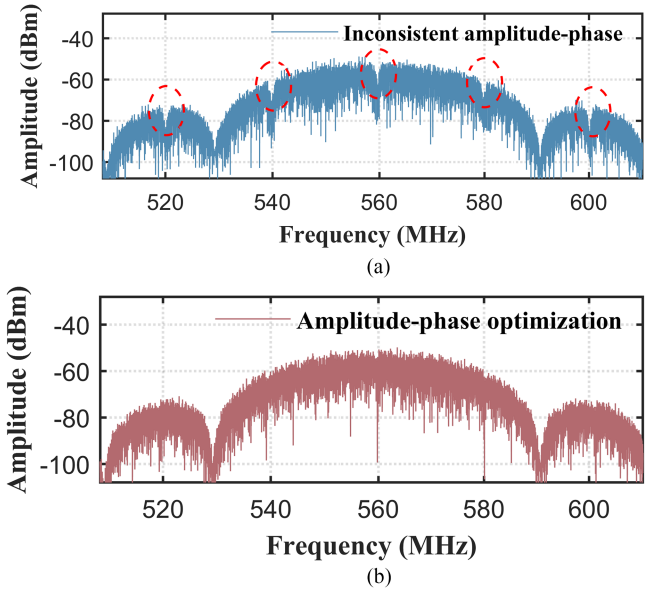

Fig. 11. MSK reconstructed signal spectrum. (a) Amplitude–phase inconsistency across subbands. (b) Amplitude and phase consistency optimization.

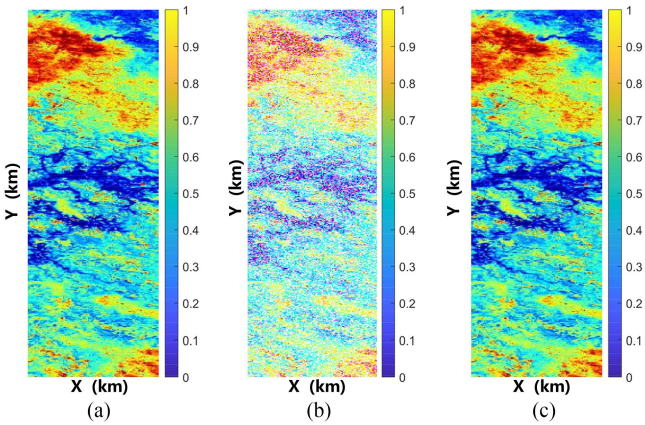

Fig. 12. Reconstruction effect of remote sensing images before and after optimization. (a) Measured spectral remote sensing images. (b) Unoptimized reconstruction distortion. (c) After optimization of amplitude and phase consistency.

remote sensing images. The simulated subband overlapping regions are set to different phase differences, corresponding to varying degrees of phase distortion. After the reconstructed signal enters the communication system, a coherent demodulation method obtains the error rate curve.

The error rate curves of the reconstructed signal across subbands under different phase distortion levels are shown in Fig. 10. Under low signal-to-noise ratio conditions, noise is the main factor affecting the communication error rate. Under the same high signal-to-noise ratio conditions, as the phase distortion level increases, the bit error rate increases. The temporal waveform distortion of the reconstructed signal across subbands will directly affect the coherent demodulation performance of the MSK signal. After phase calibration, the cross-subband reconstructed signal can better fit the theoretical error rate curve of the MSK signal. The maximum deviation from the MSK theoretical error rate does not exceed 0.1%.

VI. Experiments

To verify the amplitude–phase consistency calibration of the measured signal spectrum by the optimization method proposed, the broadband MSK signals are injected by a signal source to observe the optimization effect of the reconstructed signal spectrum.

The MSK reconstructed signal spectrum is shown in Fig. 11. Fig. 11(a) shows that the spectrum region across subbands exhibits a "depression" due to inconsistent amplitude and phase. The amplitude/phase modulation and demodulation require extremely high channel consistency in remote sensing satellite receivers. Therefore, distorted reconstructed spectrum leads to information loss and increases the BER of MSK signal demodulation. However, the optimization method for amplitude and phase consistency can effectively solve distortion and achieve approximate perfect reconstruction in Fig. 11(b).

The distortion of the signal spectrum directly affects the accuracy of the spectral image. To perform the function of the proposed multi-subband parallel processing and signal reconstruction system, the spectral remote sensing data obtained by the NASA EO-1 satellite over the Okavango Delta in Botswana are used [34]. The Hyperion sensor on EO-1 acquires data at 30-m pixel resolution over a 7.7 km strip in 242 bands covering the 400–2500 nm portion of the spectrum in 10 nm windows. The purpose of the experiment is to verify the reconstruction effect of remote sensing images before and after amplitude–phase consistency optimization using the measured remote sensing data.

Fig. 12 shows the reconstruction effect of the measured remote sensing image before and after optimization. Fig. 12(a) shows the measured spectral remote sensing image. Due to the inconsistent amplitude and phase across subbands, the demodulation performance of the reconstructed signal decreases, leading to the remote sensing image distortion in Fig. 12(b). After optimization

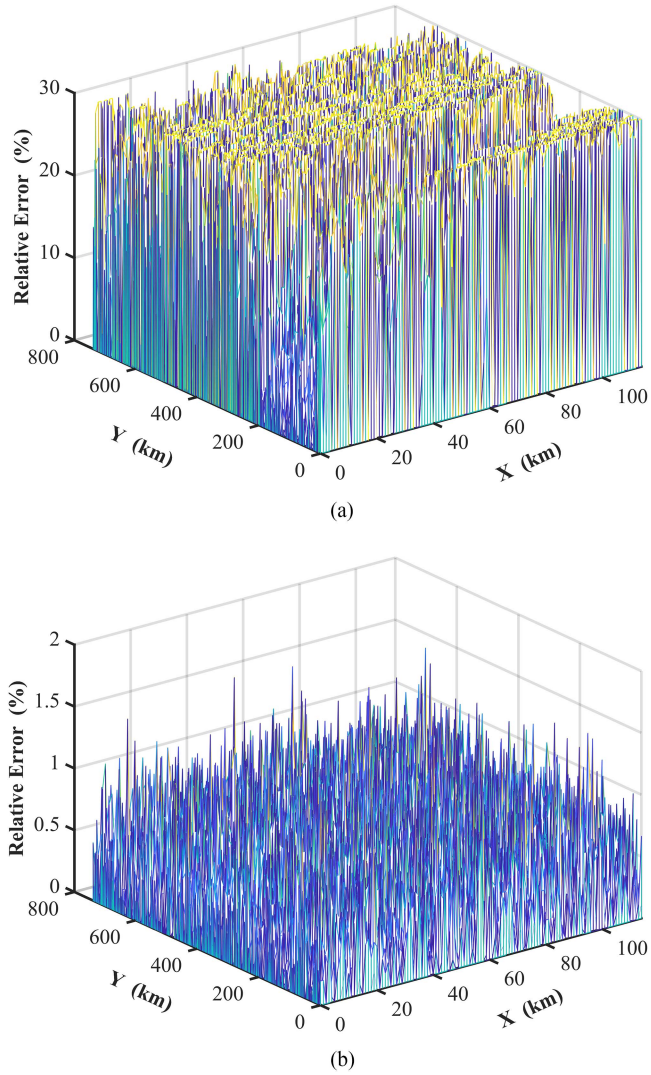

Fig. 13. Relative error of reconstruction before and after optimization. (a) Unoptimized reconstruction distortion. (b) After optimization of amplitude and phase consistency.

for amplitude and phase consistency, the reconstructed image almost recovers to the original measured image in Fig. 12(c). From the relative error, as shown in Fig. 13, the relative error before optimization can reach 30% in Fig. 13(a), while the optimization effectively reduces the relative error to 1.5% in Fig. 13(b). Therefore, the optimization method proposed has been verified to have practical engineering value through the measured data and can effectively improve the reconstruction accuracy.

VII. Discussion

To enhance the real-time reception and processing capabilities of high-resolution and high-capacity remote sensing satellite data, the subband signal reconstruction framework that combines RF analog circuits with digital processing modules is proposed. The amplitude and phase inconsistency between subbands is the main factor causing distortion in the reconstructed signal. Based on the analysis of the amplitude and phase characteristics for the receiving link, the proposed optimization method for amplitude and phase consistency is more targeted. By strongly constraining the transition band of digital filters, the reconstruction amplitude error is reduced. The phase difference introduced by analog circuits and digital modules is calibrated through digital domain phase compensation.

The multi-subband parallel and reconstruction scheme proposed in this article has universality and can be applied to fields, such as communication, radar, and satellite signal reception. It aims to provide the radio frequency bandpass sampling architecture in ultra-wideband signals and improve receiver subband consistency through amplitude–phase optimization. However, the proposed method has limitations in studying the amplitude and phase consistency of analog devices. Due to the limitations of ADC performance, it is difficult to process ultra-wideband signals in the digital processing part. Due to the limitations of ADC performance, it is difficult to have sufficient dynamic range and effective bits to process ultra-wideband signals in the digital module. Analog subband division can reduce ADC processing bandwidth, but it also reduces channel consistency. Therefore, in the future, it is necessary to propose quantitative standards for analog devices based on the reconstruction characteristics.

VIII. Conclusion

The optimization of filter amplitude–frequency response and phase calibration method can effectively improve amplitude–phase consistency between channels. The simulation results show that the amplitude and phase consistency optimization method proposed in this article effectively reduces the reconstruction error within 0.001 dB. The maximum deviation from the theoretical MSK bit error rate is not more than 0.1% after optimization of amplitude–phase consistency. The experiment uses the measured remote sensing image data to verify that the amplitude–phase consistency optimization design method proposed in this article can improve the accuracy of remote sensing images, which is feasible for engineering applications.

References

[1] M. E. Grøtte et al., "Ocean color hyperspectral remote sensing with high resolution and low latency—The HYPSO-1 CubeSat mission," *IEEE Trans. Geosci. Remote Sens.*, vol. 60, Jun. 2022, Art. no. 1000619, doi: 10.1109/TGRS.2021.3080175.

[2] H. Guo, Q. Shi, B. Du, L. Zhang, D. Wang, and H. Ding, "Scene-driven multitask parallel attention network for building extraction in high-resolution remote sensing images," *IEEE Trans. Geosci. Remote Sens.*, vol. 59, no. 5, pp. 4287–4306, May 2021, doi: 10.1109/TGRS.2020.3014312.

[3] E. Spyrakos et al., "Moving towards global satellite based products for monitoring of inland and coastal waters: Regional examples from Europe and South America," in *Proc. IEEE Latin Amer. GRSS ISPRS Remote Sens. Conf.*, 2020, pp. 363–368, doi: 10.1109/LAGIRS48042.2020.9165653.

[4] X. Tang et al., "The China ZY3-03 mission: Surveying and mapping technology for high-resolution remote sensing satellites," *IEEE Geosci. Remote Sens. Mag.*, vol. 8, no. 3, pp. 8–17, Sep. 2020, doi: 10.1109/MGRS.2019.2929770.

[5] L. Zhao et al., "China's Gaofen-3 satellite system and its application and prospect," *IEEE J. Sel. Topics Appl. Earth Observ. Remote Sens.*, vol. 14, no. 11, pp. 19–28, Oct. 2021, doi: 10.1109/JSTARS.2021.3122304.

[6] J. Kim, D. R. Utomo, A. Dissanayake, S.-K. Han, and S.-G. Lee, "The evolution of channelization receiver architecture: Principles and design challenges," *IEEE Access*, vol. 5, pp. 25385–25395, 2017, doi: 10.1109/ACCESS.2017.2772810.
[7] Y. Torres, K. Premaratne, F. Amelung, and S. Wdowinski, "An efficient polyphase filter-based resampling method for unifying the PRFs in SAR data," *IEEE Trans. Geosci. Remote Sens.*, vol. 55, no. 10, pp. 5741–5754, Oct. 2017, doi: 10.1109/TGRS.2017.2713600.
[8] F. Teng, Y. Jiao, W. Yang, J. Yan, Z. Gao, and Z. Lu, "Multiphase parallel demodulation for remote sensing satellite data transmission—Filter bank based on WOLA structure," *IEEE J. Sel. Topics Appl. Earth Observ. Remote Sens.*, vol. 15, no. 9, pp. 556–565, Aug. 2022, doi: 10.1109/JSTARS.2022.3201251.
[9] T. Li, Tianzhu Liu, Y. Wang, X. Li, and Y. Gu, "Spectral reconstruction network from multispectral images to hyperspectral images: A multitemporal case," *IEEE Trans. Geosci. Remote Sens.*, vol. 60, Aug. 2022, Art. no. 5535016, doi: 10.1109/TGRS.2022.3195748.
[10] J. Dang, Z. Zhang, L. Wu, and Y. Wu, "A new framework of filter bank multi-carrier: Getting rid of subband orthogonality," *IEEE Trans. Commun.*, vol. 65, no. 9, pp. 3922–3932, Sep. 2017, doi: 10.1109/TCOMM.2017.2712178.
[11] W. Zhang, Y. Yao, Z. Zhao, W. Zhao, and J. He, "Design and FPGA implementation of a novel efficient FRM-based channelized receiver structure," *IEEE Access*, vol. 7, pp. 114778–114787, 2019, doi: 10.1109/ACCESS.2019.2935562.
[12] X. Chen et al., "Implementation of an adaptive wideband digital array radar processor using subbanding for enhanced jamming cancellation," *IEEE Trans. Aerosp. Electron. Syst.*, vol. 57, no. 2, pp. 762–775, Apr. 2021, doi: 10.1109/TAES.2020.3042764.
[13] T. K. Sjögren et al., "Suppression of clutter in multichannel SAR GMTI," *IEEE Trans. Geosci. Remote Sens.*, vol. 52, no. 7, pp. 4005–4013, Jul. 2014, doi: 10.1109/TGRS.2013.2278701.
[14] X. Yang, S. Li, Q. Liu, T. Long, and T. K. Sarkar, "Robust wideband adaptive beamforming based on focusing transformation and steering vector compensation," *IEEE Antennas Wireless Propag. Lett.*, vol. 19, no. 12, pp. 2280–2284, Dec. 2020, doi: 10.1109/LAWP.2020.3029950.
[15] C. S. Murthy and K. Sridevi, "Optimized DA-reconfigurable FIR filters for software defined radio channelizer applications," *Circuit World*, vol. 47, no. 3, pp. 252–261, Nov. 2021.
[16] M. Jasinski, L. Yang, A. Lamecki, R. Gómez-García, and M. Mrozowski, "RF multi-functional input-reflectionless dispersive-delay structure with sharp-rejection filtering using channelization techniques," *IEEE Trans. Circuits Syst. II, Express Briefs*, vol. 70, no. 4, pp. 1410–1414, Apr. 2023, doi: 10.1109/TCSII.2022.3228391.
[17] T. Q. Nguyen and P. P. Vaidyanathan, "Two-channel perfect-reconstruction FIR QMF structures which yield linear-phase analysis and synthesis filters," *IEEE Trans. Acoust., Speech, Signal Process.*, vol. 37, no. 5, pp. 676–690, May 1989, doi: 10.1109/29.17560.
[18] S. R. Srinivasavaradhan, M. Du, S. N. Diggavi, and C. Fragouli, "Algorithms for reconstruction over single and multiple deletion channels," *IEEE Trans. Inf. Theory*, vol. 67, no. 6, pp. 3389–3410, Jun. 2021, doi: 10.1109/TIT.2020.3033513.
[19] Y. Jang, G. Kim, B. Park, and H. Lim, "Generalized polyphase digital channelizer," *IEEE Trans. Circuits Syst. II, Express Briefs*, vol. 68, no. 10, pp. 3366–3370, Oct. 2021, doi: 10.1109/TCSII.2021.3069887.
[20] F. J. Harris, *Multirate Signal Processing for Communication Systems*. London, U.K.: River Publisher, 2021.
[21] S. Sudharman and T. S. Bindiya, "Design of power efficient variable bandwidth non-maximally decimated FRM filters for wideband channelizer," *IEEE Trans. Circuits Syst. II, Express Briefs*, vol. 66, no. 9, pp. 1597–1601, Sep. 2019, doi: 10.1109/TCSII.2018.2888897.
[22] S. Patel, R. Dhuli, and B. Lall, "Analysis of signals via non-maximally decimated non-uniform filter banks," *IEEE Trans. Circuits Syst. I, Reg. Papers*, vol. 66, no. 10, pp. 3882–3895, Oct. 2019, doi: 10.1109/TCSI.2019.2914302.
[23] W. A. Martins, M. R. B. Shankar, and B. Ottersten, "Oversampled DFT-modulated biorthogonal filter banks: Perfect reconstruction designs and multiplierless approximations," *IEEE Trans. Circuits Syst. II, Express Briefs*, vol. 67, no. 11, pp. 2777–2781, Nov. 2020, doi: 10.1109/TCSII.2019.2962462.
[24] R. Kobayashi, T. Abrao, and A. Mussi, "Near-perfect reconstruction short length pulses for FBMC systems: Re-optimising OFDP design via semi-definite programming," *IET Signal Process.*, vol. 13, no. 8, pp. 701–707, Oct. 2019.
[25] N. Fu, S. Jiang, L. Deng, and L. Qiao, "Successive-phase correction calibration method for modulated wideband converter system," *IET Signal Process.*, vol. 13, no. 6, pp. 624–632, Aug. 2019.
[26] B. Tian and C. X. Li, "Low complexity satellite borne channelizer with approximate accurate reconstruction," *Syst. Eng. Electron. Technol.*, vol. 41, no. 6, pp. 1395–1401, Jul. 2019.
[27] X. Chen, F. J. Harris, E. Venosa, and B. D. Rao, "Non-maximally decimated analysis/synthesis filter banks: Applications in wideband digital filtering," *IEEE Trans. Signal Process.*, vol. 62, no. 4, pp. 852–867, Feb. 2014, doi: 10.1109/TSP.2013.2295549.
[28] X. Liu, W. Li, J. Wei, and L. Cheng, "Adaptable hybrid filter bank analog-to-digital converters for simplifying wideband receivers," *IEEE Commun. Lett.*, vol. 21, no. 7, pp. 1525–1528, Jul. 2017, doi: 10.1109/LCOMM.2017.2690281.
[29] S. Taheri, M. Ghoraishi, P. Xiao, L. Zhang, and Y. Xin, "Square-root Nyquist filter design for QAM-based filter bank multicarrier systems," *IEEE Trans. Veh. Technol.*, vol. 67, no. 9, pp. 9006–9010, Sep. 2018, doi: 10.1109/TVT.2018.2847730.
[30] R. T. Kobayashi and T. Abrão, "FBMC prototype filter design via convex optimization," *IEEE Trans. Veh. Technol.*, vol. 68, no. 1, pp. 393–404, Jan. 2019, doi: 10.1109/TVT.2018.2879856.
[31] P. M. Krishna and T. P. S. Babu, "Polyphase channelizer demystified [lecture notes]," *IEEE Signal Process. Mag.*, vol. 33, no. 1, pp. 144–150, Jan. 2016, doi: 10.1109/MSP.2015.2477423.
[32] J. C. Richard, M. K. Chandra, and R. M. Raafat, *Multiplexer Theory and Design*. Hoboken, NJ, USA: Wiley, 2018.
[33] S. Negovan, S. Nikola, and P. Goran, "Group delay equalization of polynomial recursive digital filters in maximal flat sense," *J. Circuits, Syst. Comput.*, vol. 28, no. 10, pp. 77–89, Apr. 2019.
[34] M. Graña, M. Veganzons, and B. Ayerdi, "Hyperspectral remote sensing scenes: Botswana: Concatenated, 2001 to 2004," 2001. [Online]. Available: https://www.ehu.eus.com

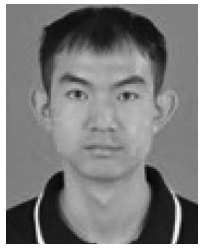

Ze Wang received the B.S. degree in automation from the Beijing Institute of Technology University, Beijing, China, in 2019, and the M.S. degree in instrumentation and science and technology from the National University of Defense Technology University, Changsha, China, in 2022. He is currently working toward the Ph.D. degree in electrical engineering with Naval Engineering University, Wuhan, China.

His current research interests include geomagnetic data processing, and the satellite communication and reception.

Fangmin He received the B.S. degree in communication engineering, the M.S. degree in electromagnetic field and microwave technology, and the Ph.D. degree in communication and information systems from the Huazhong University of Science and Technology, Wuhan, China, in 2004, 2007, and 2010, respectively.

In 2010, he joined the Research Institute of Power Electronic Technology, Naval University of Engineering, as a Lecturer, and since 2019, he has been a Professor of electrical engineering. His current research interests include communication signal processing and remote sensing image processing.

Zhong Yang received the B.S. and Ph.D. degrees in communication engineering from the Nanjing University of Science and Technology, Nanjing, China, in 2013 and 2021, respectively.

He is currently a Lecturer with the Naval University of Engineering, Wuhan, China. His research interests include machine learning, remote sensing data acquisition, and wireless communication.

Yunshuo Zhang received the B.S. degree in automation from Harbin Engineering University, Harbin, China, in 2017, and the M.S. degree in electrical engineering in 2019 from the Naval University of Engineering, Wuhan, China, where he is currently working toward the Ph.D. degree in electrical engineering.

His current research interest focuses on the adaptive filtering algorithm.

Jin Meng received the B.S. degree from the Chongqing College of Communication, Chongqing, China, in 1999, and the M.S. and Ph.D. degrees from the Naval University of Engineering, Wuhan, China, in 2002 and 2006, respectively, all in electrical engineering.

In 2006, he joined the Research Institute of Power Electronic Technology, Naval University of Engineering, as a Lecturer, and since 2011, he has been a Professor of electrical engineering. His current research interest focuses on the theory of electromagnetic wave propagation.

Yaxing Li received the B.S. degree in communication engineering from the Harbin Institute of Technology, Harbin, China, in 2011, and the Ph.D. degree in electronic and communication engineering from Hanyang University, Seoul, South Korea, in 2017.

He is currently an Assistant Engineer with the Naval University of Engineering, Wuhan, China. His current research interests include machine learning, signal processing, and design and optimization of filters.